Disaster Monitoring by Fully Polarimetric SAR Data Acquired with ALOS-PALSAR

Yoshio Yamaguchi, *Fellow, IEEE*

***Abstract*—This paper presents scattering power decomposition images of fully polarimetric synthetic aperture radar data for disaster monitoring. Utilization of fully polarimetric data can derive full color images with red–green–blue color-coding, red for the double-bounce power, green for the volume scattering power, and blue for the surface scattering power, for which each color brightness corresponds to the magnitude. Since disaster events cause the changes of each scattering power, it becomes straightforward for everyone to recognize the changes of the color in the polarimetric decomposed images provided time series data sets are made available. After applying the four-component scattering power decomposition to fully polarimetric image data sets acquired with the Advanced Land Observing Satellite (ALOS) Phased Array type L-band Synthetic Aperture Radar (PALSAR), several images are presented for natural disaster monitoring of volcanic activity, snow accumulation, landslides and tsunami effects caused by great earthquakes. It is seen in the polarimetric decomposition images that the surface scattering power becomes predominant in most disaster areas compared to those in normal situations.**

***Index Terms*—Polarimetric synthetic aperture radar (POLSAR), radar polarimetry, scattering matrix, scattering power decomposition, disaster monitoring, Advanced Land Observing Satellite Phased Array type L-band Synthetic Aperture Radar (ALOS-PALSAR)**

I. Introduction

Radar remote sensing, especially synthetic aperture radar (SAR) observation, provides backscattering coefficient images and information over regions not directly accessible to man, or over dangerous sites, regardless of weather conditions and time. The operational advantage of radar sensing comes from the propagation characteristics of microwaves, i.e., the ability to penetrate through clouds, rain, volcanic ash and plume, dense vegetation, some types of ground surface, snow, ice, depending on frequency and material properties (dielectric constants) of the media irrespective of precipitation cover [1]. This all weather capability makes radar remote sensing the most suitable for natural disaster monitoring. Radar can be operated at all times – at day and night - and in places unsuited to optical remote sensing due to cloud cover and/or darkness.

It is known that polarimetric information can enhance radar capabilities for monitoring the earth environment. Conventional radar images are created based on the backscattering coefficient from objects using single or dual polarizations. We recognize disaster areas by the backscattering magnitude difference by comparing images before and after disaster events, or by texture information when single images are available [2]. However, it is impossible to know what type of change is created in the place of interest by the backscattering coefficient information only. Since the electromagnetic wave possesses vector nature corresponding to polarization, the scattered waves from object retain the vector information inherent to the object. By acquiring fully polarimetric data with amplitude and phases, i.e., the scattering matrix, it is possible to retrieve the object information in more detail. Polarimetric information is sensitive to orientation, shape and material constituents of objects. The principles of radar polarimetry have been investigated in many research publications [3]-[7], however, the actual data collections and its utilization are still ongoing and need to be explored for more precise monitoring of the earth environment. In this regard, it is necessary to assess on how the satellite polarimetric data serve for disaster monitoring.

Important parameters for radar sensing are center frequency, bandwidth which is directly related to resolution, and polarization. The center frequency such as for L-, C-, X-band sensors is chosen with respect to the main applications for a particular sensing scenario. The L-band sensor is primarily suited for monitoring for dense forests, tall trees, volcanic and tectonic activity, for landslides, and for some land use applications [8]-[10], due to the penetration capability and the small attenuation characteristics in lossy media at its wavelength. C-band is suited for most vegetation types and ice monitoring due to almost equivalent sizes of objects and the wavelength [11]. Since higher frequency above X-band cannot penetrate into medium, it is best suited for surface information retrieval [12]-[14]. Once the center frequency is decided, the bandwidth of radar signals determines the resolution. Typical resolutions of space-borne radars range from 1 m to 30 m depending on wavelength and bandwidth for current sensor systems (2011). The highest resolution is comparable with those of optical sensors [15].

Although many air-borne SAR systems have demonstrated their capabilities, they cannot routinely observe the earth environment. For the purpose of monitoring the earth environment routinely, the first satellite "*Advanced Land Observing Satellite (ALOS)*" was launched in January 2006

Manuscript received October 10, 2011; revised Jan. 26, 2012; accepted April 6, 2012. This work was supported in part by the Ministry of Education, Japanese Government under Grant "Space Sensing Project".

Y. Yamaguchi is with Niigata University, Niigata, 950-2181, Japan. (e-mail: yamaguch@ ie.niigata-u.ac.jp).

and observed the earth surface until April 2011 [9]. This satellite carried a "*Phased Array type L-band Synthetic Aperture Radar (PALSAR)*" which was equipped to collect fully polarimetric image data sets. Although the fully polarimetric mode was designed as being experimental, it had acquired imagery for more than 274,000 scenes collected in parts over the entire globe during its period of operation, demonstrating the usefulness and effectiveness of fully polarimetric information. This paper presents some imaging results of the fully polarimetric mode of the ALOS-PALSAR sensor for disaster monitoring of recent natural hazard events such as volcanic activity, snow accumulation, landslides and tsunami effects caused by great earthquakes.

II. Experimental Verification of Polarimetric Feature Extraction

Polarimetric synthetic aperture radar measures the scattering matrix [S]. In the horizontal (H) and vertical (V) polarization basis, the scattering matrix can be expressed as

$$[\,S\,(HV)\,] = \begin{bmatrix} S_{HH} & S_{HV} \\ S_{VH} & S_{VV} \end{bmatrix}. \qquad (1)$$

Between 1988 and 2004, intensive data collections were carried out by the first polarimetric air-borne SAR system, the AIRSAR, developed by the NASA Jet Propulsion Laboratory, USA [8]. These observations brought us many new findings and revealing scientific results. The polarimetric analyses of AIRSAR data as well as the following SIR-C/X-SAR data demonstrated the following experimental evidences as shown in Fig.1.

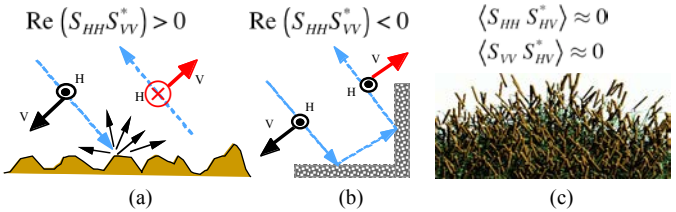

Fig. 1 Scattering mechanisms by experimental verification: (a) Surface scattering, (b) Double bounce scattering, (c) Reflection symmetry condition for natural distributed target.

1) *Surface scattering*: The scattering mechanism is mainly caused by rough surfaces such as bare soil, volcano summits, sea surfaces, agricultural fields, etc. The specific features are that the co-pol. components (S_{HH} and S_{VV}) of the scattering matrix are almost in phase, although the magnitude may be different. This behavior is characterized by

$$\mathrm{Re}\left(S_{HH}S_{VV}^*\right) > 0\,. \qquad (2)$$

2) *Double bounce scattering:* Right angle structures such as road surfaces and building walls, river surfaces and bridge structures, etc, are causing the double bounce scattering. This scattering mechanism is characterized by the fact that S_{HH} and S_{VV} are out of phase, and it can be written as

$$\mathrm{Re}\left(S_{HH}S_{VV}^*\right) < 0\,. \qquad (3)$$

3) *Volume scattering:* Naturally distributed vegetation, such as forests in topographically flat areas, provides numerous scattering centers. The ensemble average of the cross-correlation between the co-pol. and cross-pol. channel yields the so-called "Reflection Symmetry" condition,

$$\left\langle S_{HH}\, S_{HV}^* \right\rangle \approx \left\langle S_{VV}\, S_{HV}^* \right\rangle \approx 0\,. \qquad (4)$$

where <...> indicates ensemble average.

This experimental evidence, although limited in its higher order polarimetric phase characteristics, was utilized thereafter in many decomposition theorems [16]-[33] and was also incorporated into the four-component scattering power decomposition method [33] which follows.

III. Four-Component Scattering Power Decomposition

If we transform scattering matrix (1) into the covariance or coherency matrix representations and define the ensemble average, which retains the second order statistics of polarimetric information, we can have 9 independent polarization parameters [4]-[7]. The coherency matrix after ensemble averaging is written as (5).

The information included in the coherency matrix and the covariance matrix is the same because of their unitary transformation relation. There are several decomposition methods to retrieve information from the covariance or coherency matrix. Since the coherency matrix is a 3 x 3 positive definite matrix, there exit 3 eigenvalues. The Entropy/Alpha/Anisotropy decomposition is one of the most frequently used methods [17]-[18]. On the other hand, using physical scattering model-based decompositions it is more straightforward to interpret the final imaging result because the experimental evidence is incorporated in the model-based approach. The pioneering work in the model-based decomposition was presented by Freeman and Durden [19] by

$$\langle [\,T\,] \rangle = \frac{1}{2} \begin{bmatrix} \left\langle |\,S_{HH} + S_{VV}\,|^2 \right\rangle & \left\langle (S_{HH} + S_{VV})\,(S_{HH} - S_{VV})^* \right\rangle & \left\langle 2\,S_{HV}^*\,(S_{HH} + S_{VV}) \right\rangle \\ \left\langle (S_{HH} - S_{VV})\,(S_{HH} + S_{VV})^* \right\rangle & \left\langle |\,S_{HH} - S_{VV}\,|^2 \right\rangle & \left\langle 2\,S_{HV}^*\,(S_{HH} - S_{VV}) \right\rangle \\ \left\langle 2\,S_{HV}\,(S_{HH} + S_{VV})^* \right\rangle & \left\langle 2\,S_{HV}\,(S_{HH} - S_{VV})^* \right\rangle & \left\langle 4\,|\,S_{HV}\,|^2 \right\rangle \end{bmatrix} \qquad (5)$$

introducing the three-component decomposition approach. To date, a significant amount of research has been carried out on the model-based decomposition techniques [20]-[33]. We make use of the four-component scattering power decomposition [27], [33], and review it briefly.

Fig. 2 shows the four-component scattering power decomposition concept. The acquired coherency matrix is rotated to minimize the T33 component of (5) at the first stage, then, the rotated matrix is expanded into 4-sub matrices representing surface-, double-bounce-, volume-, and helix scattering mechanisms. After equating all elements, we can determine each scattering power separately for which the details of the decomposition scheme are given in [33].

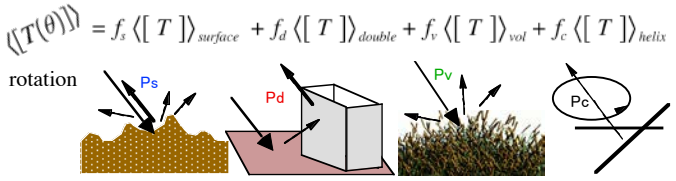

Fig. 2 Four-component scattering power decomposition with rotation of coherency matrix.

It is important to note that this decomposition method utilizes almost all important polarimetric parameters for the decomposition, accounting for 6 parameters out of 8. In this decomposition, the number of polarimetric parameters is reduced from 9 to 8 by the rotation of the coherency matrix [33]. By this four-component decomposition, it is possible to retrieve each scattering power in an imaging window under investigation. The polarimetric decomposition powers can be quantitatively analyzed, or can be qualitatively composed to create full color imagery for visual interpretation.

IV. ALOS PALSAR Quad-Pol. Imaging Results

In this section, color-coded images of ALOS-PALSAR data sets are demonstrated for visual interpretation of disaster monitoring including volcanic activity, snow cover mapping, landslides and earthquakes. ALOS-PALSAR, launched by Japan Aerospace Exploration Agency (JAXA), is the space-borne fully polarimetric SAR and has operated from 2006 to 2011. Although the fully polarimetric mode was designated experimental and as such implemented very rarely, it still was able to acquire data sets covering more than 274,000 scenes worldwide [9].

The main features are,

Frequency: L-band (1.27 GHz)

Resolution: 30 m in the range and 5 m in the azimuth direction for Single Look Complex data

Angle of incidence: 21.5 and 23.1 degrees.

The window size for ensemble averaging in the image processing is chosen as 2 in the range direction and 12 in the azimuth direction, which corresponds to 60 m by 60 m on ground [33]. After decomposing scattering powers, a number of color-coded images are created to show full-color images with *Red: double bounce scattering, Green: volume scattering,* and *Blue: surface scattering.* In color-code rendering, we used the same measure that each power magnitude is proportional to the color brightness. After composing of a color-coded RGB image, the whole image brightness is changed to a certain level in order to be seen clearly, but keeping the same brightness level to other RGB images for comparison of time series data. The images shown in this paper are based on the same measure. Since each color directly corresponds to a scattering mechanism and power, it is easy to interpret the images by relating typical objects as shown in the Table 1.

TABLE 1. Scattering mechanism and its correspondence to typical objects

Color	scattering type	typical objects	other candidates
	Double bounce scattering	man-made objects, houses, buildings road with fence	isolated trees, vegetation in row
	Volume scattering	vegetation, oriented buildings with respect to radar illumination	edges that produce the cross polarized *HV* component
	Surface scattering	bare soil surface, crop field, snow, volcano ashes	Sea surface, water body

A. Volcanic Activity

Fig. 3 shows Miyake-jima volcano image before and after eruption of SO_2 gas during the observation period Nov. 6 to Nov. 24, 2008. The island is located at 34.08N, 139.53E, Tokyo, Japan. Compared to Fig. 3(a) 20081009 (#ALPSRP144262920) image, we can see more blue caused by the surface scattering in 20081124 (#ALPSRP150972920) image. This implies that surface scattering increased due to deposition of volcanic ash; and that SO_2 gas at least partially defoliated the vegetation making it more transparent at L-band frequencies which also created more barer surface scattering. Therefore the change in blue color area indicates the effect caused by this SO_2 gas eruption. Man-made structures such as houses are easily recognized by red color and remain the same in these two images.

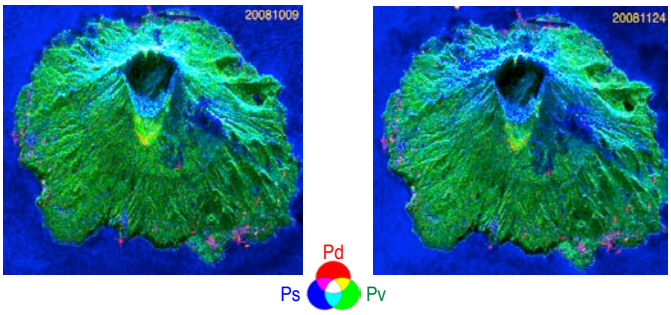

Fig 3. Volcano eruption at Miyake-jima (34.08N, 139.53E), Tokyo, Japan. (a) Data take on 20081009 (#ALPSRP144262920) before SO2 gas eruption, (b) Data take on 20081124 (#ALPSRP150972920) after the gas eruption, Angle of incidence = 21.5 degrees.

Fig. 4 shows another example of volcano "Shinmoedake" images before and after eruption, which occurred intermittently during Jan. 19 - Feb. 14, 2011. The volcano is

located 31.54 N, 130.54 E in southern Kyushu, Japan. For comparison of images, Google earth image is shown in Fig. 4 (a), which includes many volcano mouths in the Kirishima volcano region of nearby "Ebino-city". These topography details are easily recognized by polarimetric decomposed images in Fig. 4 (b) and (c). Since the image (b) is acquired on June 10, 2009 before eruption, we can see more vegetation scattering (green) than those in the image (c) on March 16, 2011. After the eruption, volcanic ash covered the surrounding area and suppressed the volume scattering by vegetation. This caused stronger surface scattering compared to other scattering mechanisms, resulting in blue color increase. Again, it is useful to monitor volcanic activities by the ALOS-PALSAR fully polarimetric POLSAR because at L-band frequency radar waves can penetrate volcanic smoke in the sky and obtain information of volcanic activities beneath the ash covered vegetation, as shown in Fig. 4 (c). It is possible to check the area covered by the volcanic ash easily.

B. Snow Accumulation

Niigata prefecture, Japan, is known as snow country. The snowpack depth changes year by year, however, it may be as much as 4 m and more in a heavy snow year. The amount of accumulated snow or snowpack depth is one of the important hydrological issues for rice/crop planting or hydrological dam water storage. By implementation of time series data analyses, it becomes possible to monitor the annual amount of snow as shown in Fig. 5. From left to right, the images clearly display the effect of snow-cover in the surface scattering power. The left-most image Fig. 5(a) shows a snow-free situation, whereas (b) is taken when the snow is wet in March. At a similar acquisition time of (c), one year later, much more blue color is displayed as a cause of snow accumulation. In the region around letter "A" in Fig. 5(c) with deep blue color, the snow depth became 4 m in Feb and 3 m at the time of data acquisition. Therefore, comparison with time series data can provide the information of snow remaining in mountainous areas year by year. The wide area monitoring of the four-component decomposition is one of the advantages of remote sensing because local spot measurement provides only a representation of the immediate area.

For a more detailed analysis, scattering power profiles along a yellow transect "A" in Fig. 5 (a) with a snow-free situation in November and in Fig. 5 (c) with the snow-covered situation in March are compared in Fig. 6. As can be seen, the surface scattering power (Ps in blue) becomes dominant in March. However, there is no significant difference in the peak magnitude of the surface scattering power in November and in March due to different surface scattering sources (e.g. bare soil vs. snowpack). On the other hand, a significant reduction of the volume scattering power (Pv in green) and the double bounce scattering power (Pd in red) for the snow-covered situation can be seen in March. This phenomenon is caused by the absorption and scattering property of accumulated snow cover, i.e., snow cover mitigates the volume scattering caused by vegetation and the double bounce scattering from man-made structures, depending on the snow depth (see Fig. 5 (b) and (c)).

(a)

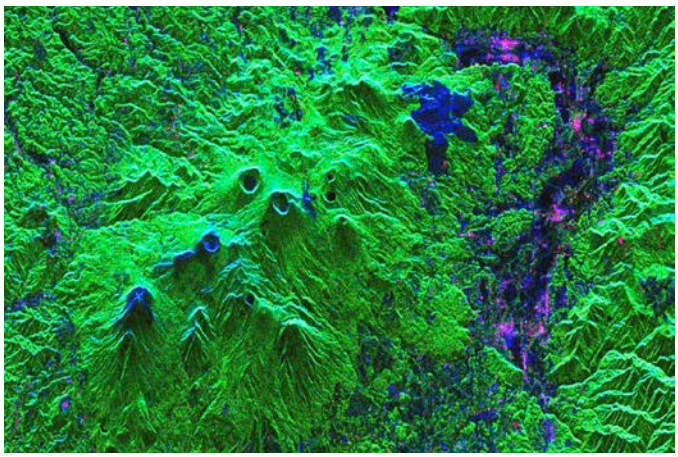

(b)

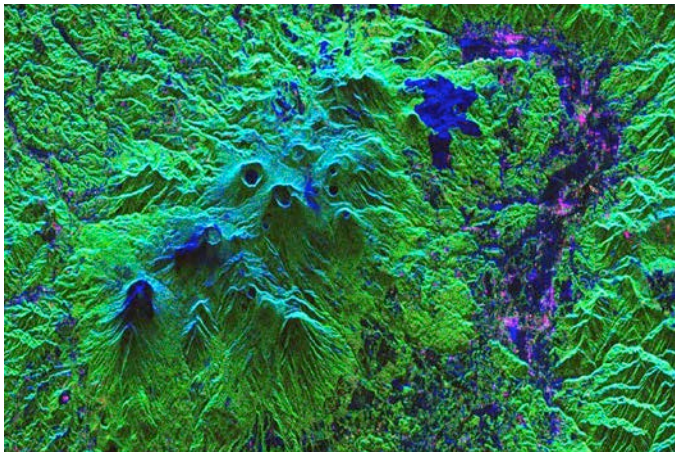

(c)

Fig. 4 Volcano eruption at Shinmoedake, Kyushu, Japan. (a) Google Earth Image, (b) Data take on 20090610 before eruption (#ALSRP179930630), (c) Data take on 20110316 after eruption (#ALPSRP273870630), Angle of incidence = 23.1 degrees.

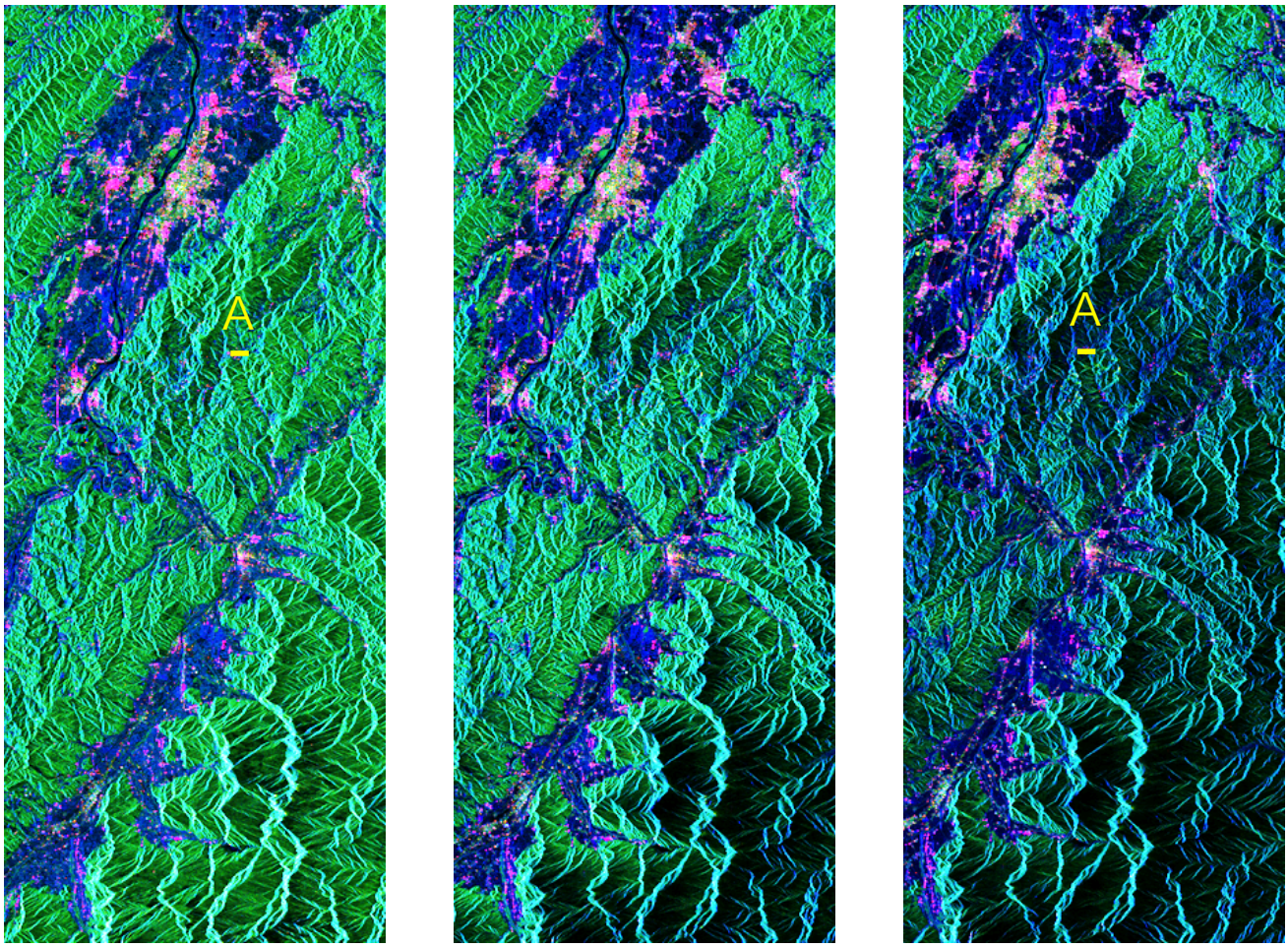

Fig. 5 Time series decomposed images over snowy country, Niigata, Japan. (a) Data take on 20081108, (b) Data take on 20090326 (c) Data take on 20100329. Angle of incidence = 21.5 degrees. Radar illumination is from the left to right

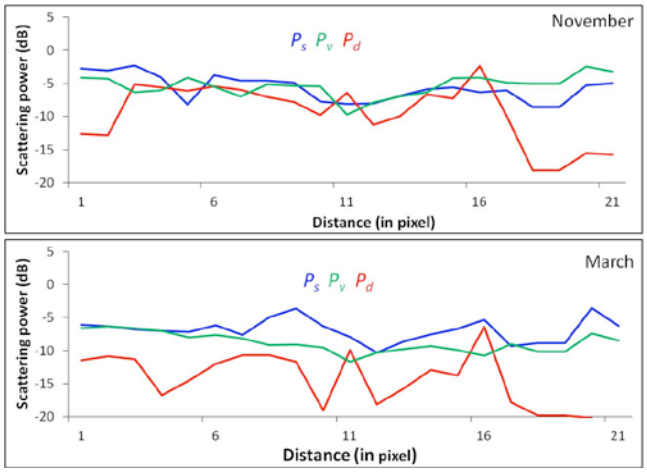

Fig. 6 Scattering power profiles along a transect "A" in Fig. 5 (a) 20081108 and (c) 20100329.

This mitigation effect leads the surface scattering to be predominant in snow-covered areas. The amount of snow may be correlated to the values of scattering powers, not only by the surface scattering power itself but also by the reduction rate of the volume and the double bounce scattering powers, quantitatively, when the snow properties including wetness, snow type, etc [34] are obtained. This will be carried out in future studies, which will also include the case of avalanche prediction in mountainous areas.

C. Landslide Identification

Large earthquakes have occurred in recent years. Earthquakes with the magnitude larger than 6, often cause landslides along mountain slopes. The landslide area can be effectively detected by implementation of fully polarimetric data. Since landslides create bare soil surfaces, and the bare soil surface reflects over a wide range of viewing angles, polarimetric radar is well suited for these observations. Fig. 7 corresponds to an image with numerous landslides after the Chuetsu earthquake in Oct. 2004, Niigata, Japan. The area has suffered from three big earthquakes with magnitudes of 6.8. It was found in the ground truth survey that most of blue colored areas in the polarimetric decomposed image were related to

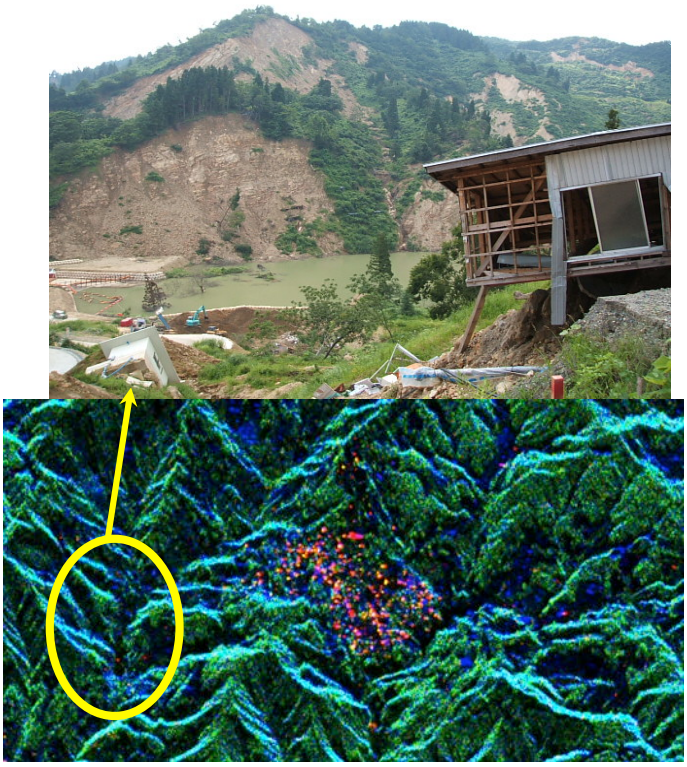

Fig. 7 Land slide caused by Chuetsu earthquake in 2004. L-band Pi-SAR decomposed image. Yellow circle shows the land slide area, which exhibits surface scattering phenomena displayed in Blue color. Most regions within blue area in this particular radar image had landslides.

landslides. The data sets had been acquired with L-band air-borne Polarimetric Interferometric Pi-SAR system [13]. Actual situation of landslide is also provided in a photo taken by the author.

Another example of landslide in Fig. 8 is a case of Sichuan earthquake, China, in 2008. The data take by ALOS-PALSAR was carried out on June 23, 2008 in its descending mode. Yellow circle indicates isolated blue areas in the slope of mountain. Compared to other areas, the dark blue exhibits strong surface scattering. We can estimate that the area has suffered from landslides because the magnitude of the earthquake exceeded more than 7.

D. Tsunami Disaster

A great earthquake with magnitude 9.0 hit East Japan on March 11, 2011. This disaster was accompanied by a huge tsunami, which attacked the eastern seashore of Tohoku area in Japan. ALOS-PALSAR had acquired fully polarimetric data over Ishinomaki area before and after the earthquake on 20101121 and 20110408, respectively. The area was heavily destroyed not only by the earthquake but more so by the incoming and the retreating tsunami waves. The major part of Ishinomaki-city and neighboring Onagawa-cho were completely destroyed and washed out by the tsunami. Fig. 9 shows the corresponding ALOS-PALSAR polarimetric images of Ishinomaki-city before and after the earthquake together with ground truth data. Although the second data take (April

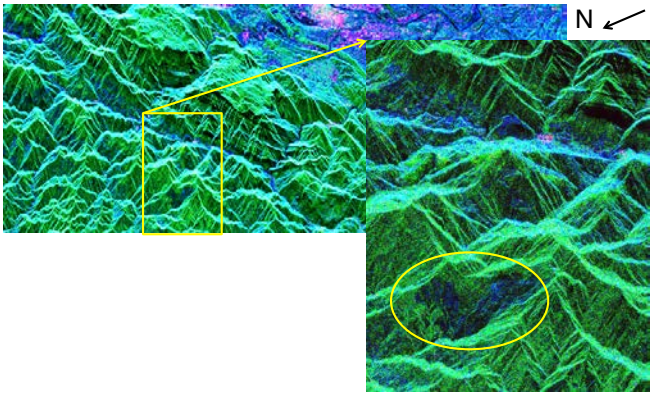

Fig.8 Land slide caused by Sichuan earthquake in 2008. Yellow circled areas along mountain slope exhibit the surface scattering in Blue color. Data no. ALPSRP128522970 acquired on 20080623.

8) was 28 days after the earthquake (March 11), it is possible to confirm several changes: red color (man-made) area turned into blue color (surface scattering due to completely washed out area due to the impact of the tsunami) near by the seashore in Fig. 9 (a) and (b). The ground truth was carried out by the Association of Japanese Geographers and the Geospatial Information Authority of Japan, respectively. Fig. 9 (c) shows the extent of the disaster area with blue indicating destruction by tsunami and with orange indicating flooding by tsunami. The legend color "*orange*" in Fig. 9 (c) denotes the flooded area where the tsunami hit. But there were still remaining some buildings/houses and man-made structures after the tsunami. The "blue" color in Fig. 9 (c) denotes the area where almost all buildings/houses and man-made structures had collapsed or were destroyed and washed away by the tsunami, leaving bare surface on the ground. We can observe corresponding features very well in Fig. 9 (b) and (c).

For quantitative comparisons before and after the disaster, various polarimetric scattering powers in dB are illustrated in Fig. 10 along a transect "B" of Fig.9. The polarimetric power indexes in Fig. 10 are

$|S_{HH}|^2, |S_{VV}|^2, |S_{HV}|^2$ in (a) and (d)

$\frac{|S_{HH}+S_{VV}|^2}{2}, \frac{|S_{HH}-S_{VV}|^2}{2}, 2|S_{HV}|^2$ in (b) and (e)

Ps, Pv, Pd, Pc in (c) and (f)

The horizontal axis corresponds to pixel range along the transect "B". The pixel distance from 4 to 12 corresponds to the destroyed area, washed away by the tsunami. It is seen that polarimetric channel powers have similar trend in (a) and (e) and that it is difficult to detect the change due to disaster. The Pauli basis index in (b) and (e) shows the power $\frac{|S_{HH}+S_{VV}|^2}{2}$ is strong indicating the surface scattering dominant in the pixel distance from 4 to 12. By comparing all these power profiles carefully, it is seen that Ps, Pv, Pd, Pc in (c) and (f) provide the change before and after the disaster most significantly, i.e., the double bounce power Pd is significantly reduced in (f) rather than $\frac{|S_{HH}-S_{VV}|^2}{2}$ in (e). In addition, Ps, Pv, Pd, Pc profiles show the most detailed scattering information along the transect "B". Since the value of Pc is much smaller than those of other powers and RGB color-coding is employed to

create images, the helix scattering power Pc is omitted to display throughout the polarimetric scattering power images in this paper.

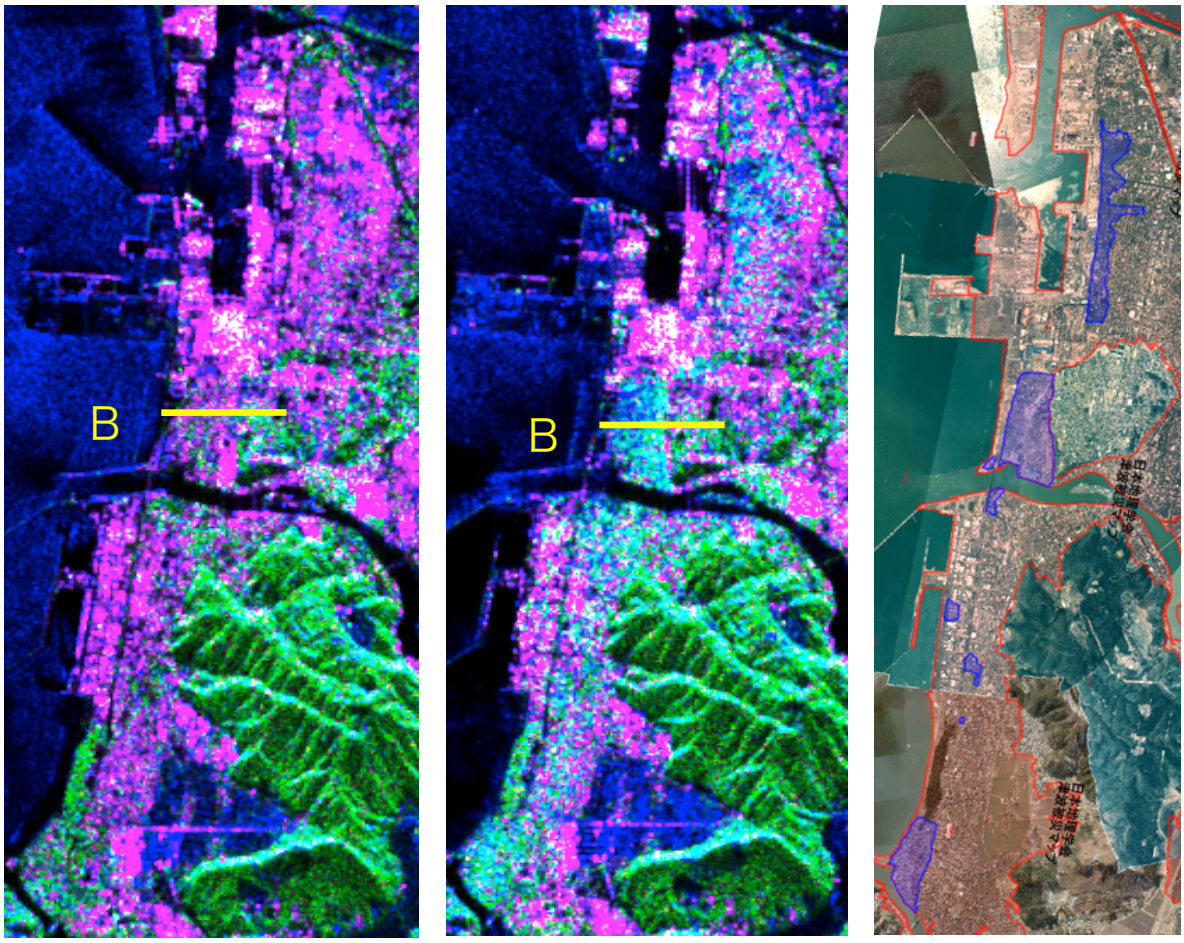

(a) (b) (c)

Fig. 9 Ishinomaki area suffered from tsunami caused by great earthquake of East Japan 2011. (a) before; (b) after the earthquake and tsunami. Color composite images are generated by scattering power decomposition with surface scattering (Blue), double bounce scattering (Red), and volume scattering (Green); (c) ground truth data: Blue color areas show totally destroyed areas by tsunami. Orange color denotes the area flooded by tsunami. Ground truth provided by Association of Japanese Geographers, and Geospatial Information Authority of Japan, respectively.

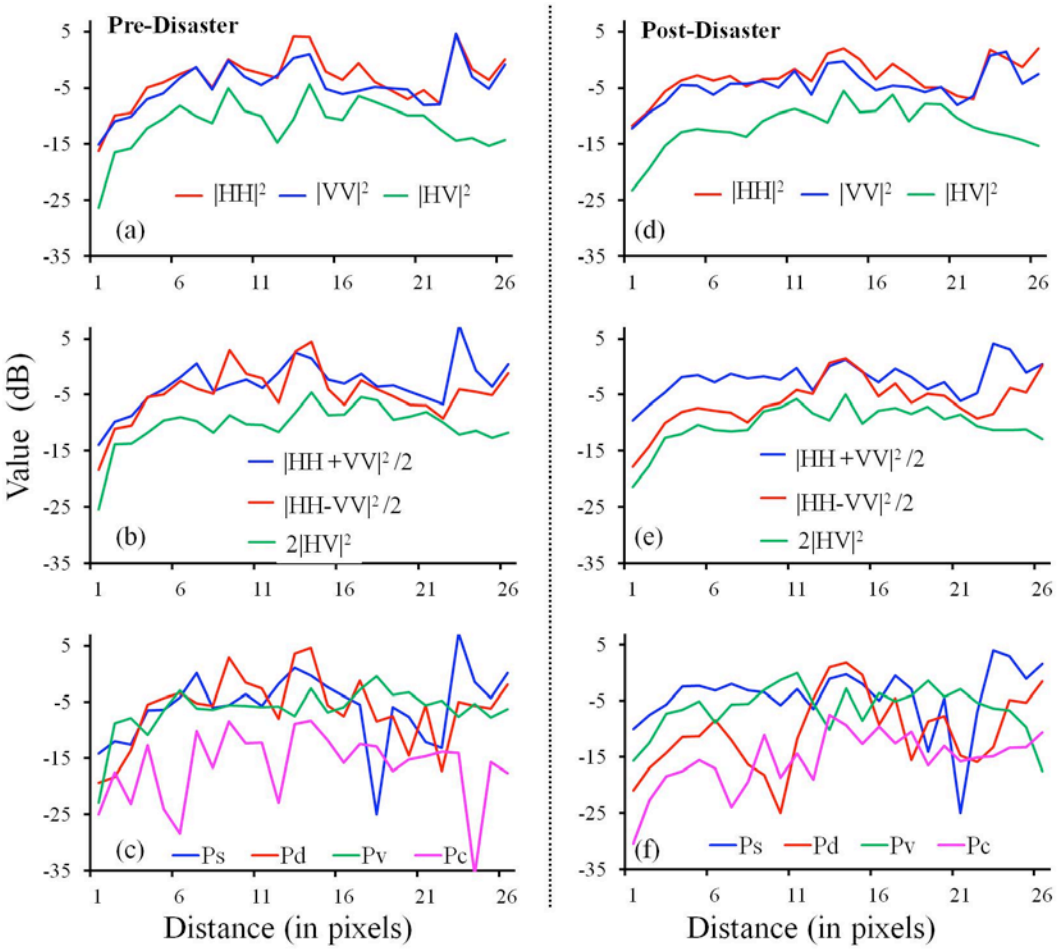

Fig. 10 Polarimetric scattering power profiles along a transect "B" of Fig. 9 (a) and (b).

Onagawa-cho image in Fig. 11 (a) lost red color of the double bounce scattering power in Fig. 11 (b), indicating that almost all of the man-made structures were destroyed by the earthquake and the tsunami. Purple (blue + orange) color areas in the ground truth image of Fig. 11 (c) show collapsed and destroyed areas by tsunami. The polarimetric decomposed image of Fig. 11 (b) seems to display exact correspondence to the ground truth image (c).

Final example of the disaster image is around the mouth of Kitakami-river near Onagawa-cho as shown in Fig. 12. Since this area is sparsely populated, there are not so much houses or man-made structures indicating less red spots in Fig. 12 (a). Yet, the red spots are still reduced in Fig. 12 (b) by tsunami disaster. In addition, it is possible to see at the center bottom of Fig.12 that a small green area has been completely wiped out by the tsunami. The river as well as its surrounding shows the surface scattering to be predominant after the tsunami tide.

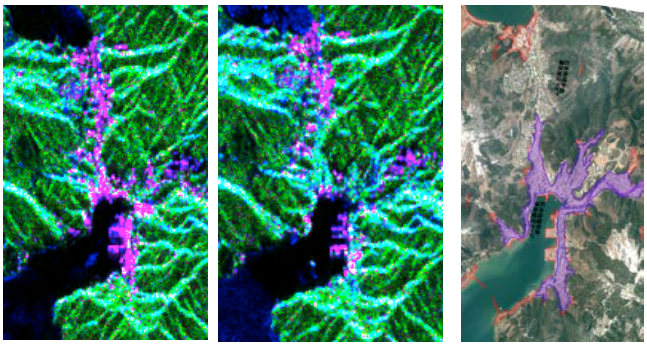

(a) (b) (c)

Fig. 11 Onagawa-cho suffered from tsunami caused by great earthquake of East Japan 2011. (a) before, (b) after the earthquake and tsunami. The parameters are the same as those of Fig. 9.

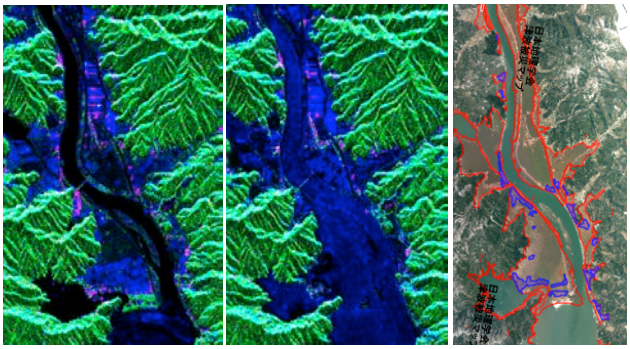

(a) (b) (c)

Fig.12 The mouth of Kitakami-river suffered from tsunami caused by great earthquake of East Japan 2011. (a) before, (b) after the earthquake and tsunami. The parameters are the same as those of Fig. 9.

V. Discussion

Several polarimetric decompositions were presented to show the usefulness and effectiveness of fully polarimetric SAR data for disaster monitoring. Compared to the conventional amplitude radar imagery, fully polarimetric images (Fig. 3 to Fig. 12) are easily comprehended by everybody because of the full color-coding. The space-borne ALOS-PALSR provided us with very precious data sets for monitoring the earth surface. We have applied the scattering power decomposition to create color-coded imagery. This method provides a straightforward method for change detection or comparison over the region of interest, especially when time series data sets are available.

Most of disaster areas highlighted tend to exhibit that surface scattering is predominant compared to the pre-disaster situation. Since many natural hazards create bare soil on the top of the underlying surface, and since volcanic ash or snow accumulation mitigates the volume and double bounce scattering powers, a polarimetric decomposed image tends to show an increased surface scattering power. This color change from red (double bounce scattering) to blue (surface scattering) can be a good indicator for general disaster monitoring. However, it is necessary to carry out quantitative analyses for more accurate assessments.

VI. Concluding Remarks

In this paper, some scattering power decompositions of fully polarimetric SAR data are displayed to show the effectiveness and usefulness of its implementation for disaster monitoring. Examples of polarimetric decompositions for volcanic activity, snow cover, landslide and tsunami disasters were shown using L-band fully polarimetric SAR data. Color-coded images of scattering power decomposition serve as a simple approach to identify areas of interest, since color represents the scattering mechanisms directly. It is found that most disaster areas show increasing blue color compared to those in pre-disaster situations. Therefore, the color change from red (double bounce scattering) to blue (surface scattering) will be a good indicator for general disasters. While not highlighted in this paper, flood monitoring is another application well suited for polarimetric SAR imagery.

Acknowledgment

The author is grateful to Prof. K.S. Chen for providing an opportunity to report ALOS-PALSAR imaging results for disaster monitoring. The ALOS-PALSAR image data sets are provided by the Japan Aerospace Exploration Agency. We appreciate graduate students, Mr. A. Sato and Mr. O. Shimotoso, and Dr. G. Singh, Post Doctoral Fellow, Niigata University for image processing of polarimetric data decompositions. The author is also grateful to anonymous reviewers and Prof. Wolfgang –M. Boerner for their kind suggestions to improve the manuscript.

REFERENCES

[1] F. T. Ulaby, R. K. Moore, and A. K. Fung, *Microwave Remote Sensing - Active and Passive*, vols I-III, Artech House, 1986.

[2] C. Oliver and S. Quegan, *Understanding Synthetic Aperture Radar Images*, Artech House, 1998.

[3] W. -M. Boerner eds, *Direct and Inverse Methods in Radar Polarimetry*, Part 1 and 2, NATO ASI Series, Kluwer Academic Publishers, 1992.

[4] F. M. Henderson, A. J. Lewis, *Principles & Applications of Imaging Radar, Manual of Remote Sensing*, third ed., John Wiley & Sons, Inc, 1998.

[5] Y. Yamaguchi, *Radar Polarimetry From Basics to Applications,* IEICE, 2007. 182 pages (in Japanese)

[6] J. S. Lee and E. Pottier, *Polarimetric Radar Imaging from Basics to Applications*, Boca Raton, FL: CRC Press, 2009.

[7] S. R. Cloude, *Polarisation Applications in Remote Sensing*, Oxford University Press, 2009.

[8] [Online]. Available: http://airsar.jpl.nasa.gov/ and http://southport.jpl.nasa.gov/

[9] [Online]. Available: http://www.eorc.jaxa.jp/ALOS/en/index.htm

[10] Y. Yamaguchi, W.-M. Boerner, R. Sato, and H. Yamada, "ALOS-PALSAR Quad-Pol images", I*EEE Geosci. Remote Sens. Society Newsletter*, pp. 9-12, June 2009.

[11] [Online]. Available: http://www.asc-csa.gc.ca/eng/satellites/radarsat2/

[12] [Online]. Available: http://www2.nict.go.jp/y/y221/

[13] T. Kobayashi, et al., "Airborne dual-frequency polarimetric and interferometric SAR," *IEICE Trans. Commun.*, vol. E83-B, no. 9, pp. 1945-1954, 2000.

[14] [Online]. Available: http://www.dlr.de/eo/en/desktopdefault.aspx/tabid-5725/9296_read-15979/

[15] [Online]. Available: http://www.pasco.co.jp/disaster_info/ Disaster information, PASCO Corporation,

[16] S. R. Cloude and E. Pottier, "A review of target decomposition theorems in radar polarimetry," *IEEE Trans. Geosci. Remote Sens.,* vol. 34, no. 2, pp. 498-518, Mar. 1996.

[17] S. R. Cloude and E. Pottier, "An entropy based classification scheme for land applications of polarimetric SAR," *IEEE Trans. Geosci. Remote Sens.,* vol. 35, no. 1, pp. 68-78, Jan. 1997.

[18] E. Pottier, and J. S. Lee, "Application of the <<H/A/Alpha>> polarimetric decomposition theorem for unsupervised classification of fully polarimetric SAR data on the Whishart distribution," *Proceeding of EUSAR2000*.

[19] A. Freeman and S. Durden, "A three-component scattering model for polarimetric SAR data," *IEEE Trans. Geosci. Remote Sens.,* vol. 36, no. 3, pp. 963-973, May 1998.

[20] M. Qong, "A new scattering mechanism enhancement scheme for polarimetric SAR images," *IEEE Trans. Geosci. Remote Sens.,* vol.40, no.12, pp.2582-2592, 2002.

[21] Y. Yamaguchi, T. Moriyama, M. Ishido, and H. Yamada, "Four-component scattering model for polarimetric SAR image decomposition," *IEEE Trans. Geosci. Remote Sens.,* vol. 43, no. 8, pp. 1699-1706, Aug. 2005.

[22] C. L. Martinez, E. Pottier, and S. R. Cloude, "Statistical assessment of eigenvector-based target decomposition theorems in radar polarimetry," *IEEE Trans. Geosci. Remote Sens.,* vol. 43, no. 9, pp. 2058-2074, Sept. 2005.

[23] Y. Yamaguchi, Y. Yajima, H. Yamada, "A four-component decomposition of POLSAR images based on the coherency matrix." *IEEE Geoscience Remote Sensing Letters*, vol. 3, no. 3, pp. 292-296, July 2006.

[24] Y. Yajima, Y. Yamaguchi, R. Sato, H. Yamada, W. -M. Boerner, "POLSAR image analysis of wetlands using a modified four-component scattering power decomposition," *IEEE Trans. Geosci. Remote Sens.,* vol. 46, no. 6, pp. 1667-1773, 2008

[25] J. S. Lee, D. L. Schuler, T. L. Ainsworth, E. Krogager, D. Kasilingam, W. -M. Boerner, "On the estimation of polarization orientation shifts induced by terrain slopes," *IEEE Trans. Geosci. Remote Sens.,* vol. 40, no. 1, pp. 30-41, Jan. 2002.

[26] F. Xu, and Y. Q. Jin, "Deorientation theory of polarimetric scattering targets and application to terrain surface classification," *IEEE Trans. Geosci. Remote Sens.,* vol. 43, no. 10, pp. 2351-2364, Oct. 2005.

[27] Yajima, Y. Yamaguchi, R. Sato, H. Yamada, and W. -M. Boerner, "POLSAR image analysis of wetlands using a modified four-component scattering power decomposition," *IEEE Trans. Geosci. Remote Sens.,* vol. 46, no. 6, pp. 1667-1773, June 2008.

[28] L. Zhang, B. Zou, H. Cai, and T. Zhang, "Multiple-component scattering model for polarimetric SAR image decomposition," *IEEE Geosci. Remote Sens. Letters,* vol.5, no. 4, pp. 603-607, Oct. 2008.

[29] J. S. Lee and T. Ainsworth, "The effect of orientation angle compensation on coherency matrix and polarimetric target decompositions," *IEEE Trans. Geosci. Remote Sens.*, vol. 49, no. 1, pp. 53-64, Jan. 2011.

[30] M. Arii, J. J. van Zyl, and Y. J. Kim, "Adaptive model-based decomposition of polarimetric SAR covariance matrices," *IEEE Trans. Geosci. Remote Sens.*, vol. 49, no. 3, pp. 1104 -1113, Mar. 2011.

[31] W. An, Y. Cui, and J. Yang, "Three-component model-based decomposition for polarimetric SAR data," *IEEE Trans. Geosci. Remote Sens.,* vo. 48, no.6, pp. 2732 – 2739, June 2010.

[32] R. Touzi, Deschamps, A., Rother G., "Phase of Target Scattering for Wetland Characterization Using Polarimetric C-Band SAR," I*EEE Transactions on Geoscience and Remote Sensing*, Vol. 47, pp. 3241-3261, 2009.

[33] Y. Yamaguchi, A. Sato, W. -M. Boerner, R. Sato, H. Yamada, "Four-component scattering power decomposition with rotation of coherency matrix," *IEEE Trans. Geosci. Remote Sens.,* vol. 49, no. 6, pp. 2251-2258, June 2011.

[34] T. Abe, Y. Yamaguchi, and M. Sengoku, "Experimental study of microwave transmission in snowpack," *IEEE Trans. Geosci. Remote Sens.,* vol. 28, no. 5, pp. 915-921, Sept. 1990.

Yoshio Yamaguchi (M'83 - SM'94 - F'02) received the B.E. degree in electronics engineering from Niigata University in 1976, and the M.E. and Dr. Eng. Degrees from Tokyo Institute of Technology in 1978 and 1983, respectively. In 1978, he joined the Faculty of Engineering, Niigata University. From 1988 to 1989, he was a Research Associate at the University of Illinois at Chicago. His interests are in the field of radar polarimetry, microwave sensing and imaging. He has served as Chair of IEEE GRSS Japan Chapter (02-03), Chair of URSI-F Japan (06-11), Associate editor for Asian affairs of GRSS Newsletter (03-07) and TPC co-chair of IGARSS 2011. He is a Fellow of IEICE, Japan, and a recipient of 2008 IEEE GRSS Education Award.